Supported Molybdenum Oxides for the Aldol Condensation Reaction of Acetaldehyde

Mathew J. Rasmussen,[#,1] Sean Najmi,[#,2] Giada Innocenti,[2] Andrew J. Medford,[*,2,3] Carsten Sievers,[*,2,3] J. Will Medlin[*,1]

1 Department of Chemical and Biological Engineering, University of Colorado Boulder, JSCBB D125, 3415 Colorado Avenue, Boulder, Colorado 80303, United States

2 School of Chemical & Biomolecular Engineering, Georgia Institute of Technology, Atlanta, Georgia 30332, United States

3 Renewable Bioproducts Institute, Georgia Institute of Technology, Atlanta, Georgia 30332, United States

# - Equal contribution

* - Corresponding authors: ajm@gatech.edu , carsten.sievers@chbe.gatech.edu , medlin@colorado.edu

Abstract

The (retro-)aldol condensation reaction is an important chemical transformation in the upgrading of biomass-derived compounds into fuels and valuable specialty chemicals. In this study, we found that supported molybdenum oxide (MoO_x) catalysts were active and selective for the aldol condensation of acetaldehyde to crotonaldehyde under steady-state reactor conditions. Through a combination of transmission electron microscopy (TEM), ultraviolet-visible (UV-VIS) diffuse reflectance spectroscopy, Fourier transform infrared (FTIR) spectroscopy of adsorbed pyridine, and steady-state reactor testing, we determined that highly dispersed MoO_x has a strong interaction with a γ-Al_2O_3 support resulting in optimal catalyst performance at low weight loadings. In contrast, MoO_x particles supported on SiO_2 have a weaker interaction with the support, resulting in a monotonic relationship between Mo loading and aldol condensation activity. The Lewis acid site density and strength are important parameters for predicting aldol condensation activity across all samples. The concentration of weak acid sites had a poor correlation with aldol condensation activity, most likely because these sites are too weak to activate acetaldehyde for the reaction. Medium and strong acid sites both had good correlations to aldol condensation activity. Results from X-ray absorption near edge structure (XANES) and acetaldehyde temperature programmed desorption (TPD) indicated that partially reduced MoO_x was more active for aldol condensation, but pretreatment in reducing or oxidizing environments had no significant effect on steady-state catalytic activity. Characterization of spent catalyst samples through temperature programmed oxidation (TPO) and thermogravimetric analysis (TGA) revealed that catalysts with high densities of strong acid sites tended to form more carbonaceous deposits on the surface over the course of the reaction.

KEYWORDS: reducible oxides, Lewis acid, acid site characterization, oxygen vacancy

1. Introduction

Consumption of fossils fuels for energy production is the top contributor of greenhouse gas emissions globally.[1] Switching to renewable sources/feedstocks, such as lignocellulosic biomass, can potentially alleviate many of the problems associated with the current energy portfolio.[2] Unlike other sources of renewable energy, lignocellulosic biomass has the unique advantage of being readily converted into liquid fuels which can be easily incorporated into the existing infrastructure for the transportation sector.[3] Cellulose is the most abundant component of biomass and is made up of repeating subunits of glucose molecules bound by glycosidic linkages. These carbohydrate chains can be split into individual glucose monomers through hydrolysis.[4] Sugars, such as glucose, can serve as intermediate feedstocks that can be further upgraded to fuel-grade molecules or valuable specialty chemicals. Some examples include: aqueous phase reforming of sorbitol to alkanes over a Pt/SiAl catalyst[5] and isomerization and retro aldol condensation of glucose to alkyl lactates using Sn-BEA and MoO_3[6]. Recently, there has been increased interest in the transformation of biomass-derived sugars to renewable jet fuel mixtures in the $C_9 - C_{16}$ range through a series of hydrogenation, dehydration, and aldol condensation reactions.[7,8] Careful selection of heterogeneous catalysts is key for selective transformation of sugars to value-added chemicals.

C_2 oxygenates such as ethanol and acetaldehyde are ideal candidates for studying C-C bond formation reactions to higher molecular weight products. The National Renewable Energy Laboratory recently released an overview of their state-of-the-art lignocellulosic biomass upgrading process and found that several light oxygenates, including acetaldehyde, were produced in significant quantities during the catalytic fast pyrolysis reaction.[9] These volatile compounds are not currently captured by the primary product fuel stream, but coupling reactions like aldol condensation could be utilized to upgrade these molecules into heavier fuel-grade compounds that could be readily incorporated into the liquid fuel product. Several studies have investigated the aldol condensation reaction for ethanol and acetaldehyde over a variety of metal oxide catalysts.[10–16] During the aldol condensation of acetaldehyde to crotonaldehyde, an enolate is generated by abstraction of the proton at the α-carbon position followed by addition of an adjacent acetaldehyde molecule and finally dehydration of the aldol addition product.[17] Flaherty and coworkers recently showed that this reaction most likely occurs through a mechanism involving an enolate and acetaldehyde molecule both bound to Lewis acidic Ti sites on anatase TiO_2.[18] Some studies have shown that aldol condensation reactions can lead to significant deactivation of the catalyst at high acetaldehyde pressures due to the formation of heavy, nonvolatile products.[19,20] Strong affinity of acetaldehyde on both solid acid and base sites can also cause deactivation.[20,21] As a result, a deep understanding of interactions between reactants and active sites is necessary for optimizing catalysts for the aldol condensation reaction.

We have previously shown that ethanol and acetaldehyde undergo the retro aldol condensation reaction on MoO_3 and also found that activity is enhanced when a reductive pretreatment is used.[22] A significant disadvantage of bulk MoO_3 is the inherently low surface area. One method to address this is to deposit Mo (as MoO_x) on high surface area supports like γ-Al_2O_3 and SiO_2. Characterization of Mo/Al_2O_3 and Mo/SiO_2 has shown that both materials can achieve high Mo dispersion and high surface area without forming crystalline MoO_3 phases.[23] Such catalysts have been used for many different reactions such as alkane dehydrogenation.[24–30] MoO_x can be anchored on the acid sites of γ-Al_2O_3, and DFT calculations showed that Mo – O – Al bonds were formed and surface reactivity was enhanced.[31] On the SiO_2 surface, Mo (IV) species likely form two-fold coordinated sites with a mono-oxo ligand.[32] These two different

coordination environments of MoO_x will provide insight into how properties of oxide supports may control the characteristic features of Lewis acid sites (e.g., strength, accessibility, hardness) and thus the path of surface reactions.

In this work, we show how the support and weight loading of MoO_x control the activity for aldol condensation of acetaldehyde. For heterogeneous catalysts, this reaction has typically been thought to proceed through a series of reactions (Scheme 1).[12,18,20,33] First, acetaldehyde adsorbs onto a Lewis acid site on the surface. Next, a nearby basic site removes the α-H, forming an enolate intermediate. This enolate may perform a nucleophilic attack on the carbonyl carbon of a nearby adsorbed acetaldehyde species, thereby forming the C-C bond. The resulting C_4 intermediate may then be hydrogenated and dehydrated to form the final coupling product, crotonaldehyde. To our knowledge, this is the first study that elucidates the aldol condensation of acetaldehyde over γ-Al_2O_3 and SiO_2 supported molybdenum oxide catalysts. Steady state reactions were performed to test the performance of the catalysts. Mo/Al_2O_3 and Mo/SiO_2 were characterized to rationalize how their physical makeup determines the observed reactivity.

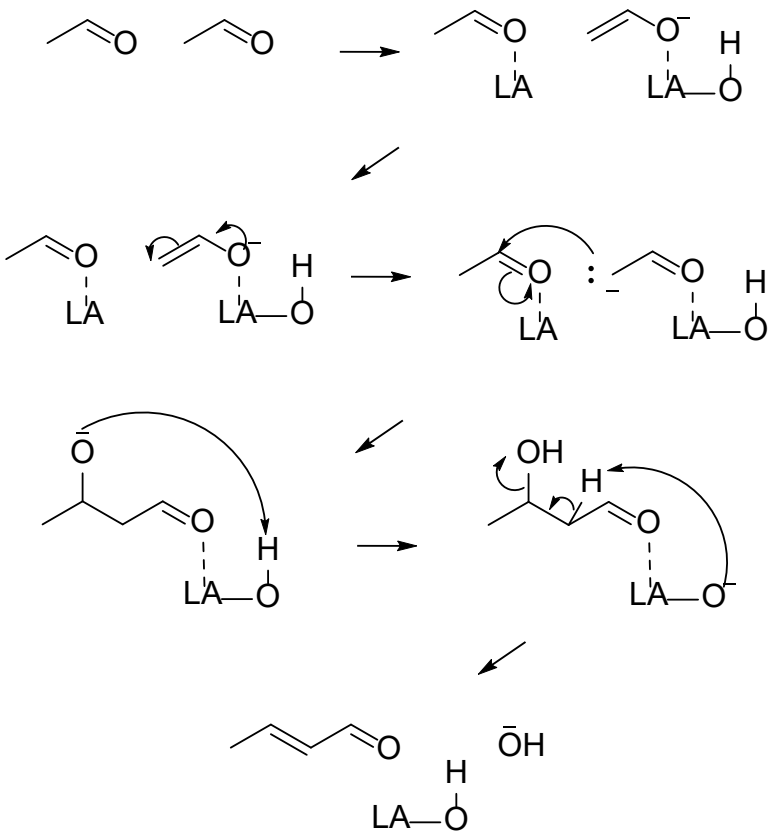

Scheme 1. Aldol condensation of acetaldehyde over a Lewis acid site.

2. Methods

Catalyst synthesis. Supported MoO_x catalysts were prepared through incipient wetness impregnation of γ-Al_2O_3 (99.997% metals basis, Alfa Aesar) and SiO_2 (HPLC grade 99.99%+, Alfa Aesar) porous supports. Ammonium molybdate tetrahydrate (99.98%, Strem Chemicals) precursor was dissolved in water at appropriate concentrations and then mixed with the corresponding support material to create catalyst

samples with a variety of Mo loadings. These samples were dried in an oven at 120 °C overnight and then calcined in air at 450 °C for 4 hours. Samples in this study are referred to as xMo/Al_2O_3 or xMo/SiO_2 where x refers to the nominal weight loading of Mo in the sample (in wt%).

Probe molecule infrared spectroscopy. The quantification of Lewis and Brønsted acid sites on the catalysts was performed using *in-situ* pyridine adsorption followed by FT-IR spectroscopy. Measurements were conducted using Thermo Scientific Nicolet iS10 by collecting 64 scans for each spectrum with a resolution of 4 cm^{-1}. Self-supported catalyst wafers were prepared and loaded into a high vacuum setup where the sample was heated to 150 °C under high vacuum for 2 h. The sample then underwent an activation step at 450 °C for 1 h. Then, the temperature was reduced to 150 °C where pyridine was introduced at a pressure of 0.1 mbar for 30 min and then allowed to equilibrate for 1 h. The sample then underwent evacuation after which a spectrum was collected. To probe the strength of acid sites, the samples were subsequently heated to 250, 350, and 450 °C, and spectra of residual pyridine were obtained at 150 °C. After the sample was removed, a 6.45 mm diameter wafer was punched out and weighed to normalize acid site concentrations. Spectra were integrated around 1540 and 1440 cm^{-1} to quantify the amount of pyridine adsorbed on Brønsted and Lewis acid sites, respectively. Molar extinction coefficients were taken from Tamura et al.[34]

These data were also used to group the Lewis acid sites on each catalyst into three general categories (weak, medium, and strong) based on their relative strengths. The number of acid sites in each group was calculated by choosing a temperature range and then subtracting the number of sites retaining pyridine at the higher temperature from the number of sites retaining pyridine at the lower temperature. Weak acid sites were assigned as the number of sites retaining pyridine up to 150 °C but not beyond 250 °C, medium sites as the number of sites retaining pyridine beyond 250 °C but not beyond 450 °C, and strong as the number of sites retaining pyridine above 450 °C.

P-value statistical significance tests and linear regression analysis were performed in OriginPro 2019 for correlations between the density of weak, medium, strong, and medium + strong acid sites to the rates of steady-state crotonaldehyde production during reaction tests for each catalyst. Adjusted R^2 values were used for comparing the linear fit models.

Catalyst evaluation. Catalyst performance was analyzed through steady state reactor experiments involving the aldol condensation of acetaldehyde (99.5%, Acros Organics) to crotonaldehyde. In a typical experiment, approximately 60 mg of catalyst sample was packed into a quartz reactor tube between two layers of quartz wool. Samples were pretreated in 36 sccm H_2 (99.999%, Airgas) at 350 °C for 1 h and purged in 36 sccm He (99.999%, Airgas) at 350°C for 30 min before cooling to 300 °C for reaction. The system was allowed to come to steady-state over 10 hours on stream, and reaction data were collected continuously using an online Agilent 7820A gas chromatograph (GC) with a DB-WAX polar column and flame ionization detector (FID). The total system pressure was equal to the ambient pressure at ~0.8 atm, and the acetaldehyde partial pressure was kept constant for each experiment at 0.07 atm. Data points for comparison were collected after 10 h on stream because the rate of deactivation had reached a low steady value for crotonaldehyde production at that timepoint (Figure S1B). Data collected at an earlier timepoint (~2.5 hours onstream) exhibited similar trends in activity with Mo loading (Figure S1A) for both the SiO_2 and γ-Al_2O_3 samples. For regeneration experiments, catalyst samples were pretreated normally and then allowed to react for 3-hour intervals before being exposed to a regeneration cycle. Each cycle consisted of either 36 sccm H_2 for 30 minutes at 350 °C or 36 sccm O_2 (99.994%, Airgas) followed by 36 sccm H_2 for 30 minutes each at 350 °C.

Aldol condensation performance was compared through the net rate of crotonaldehyde production. These "mass-time yields" are defined here as the molar flowrate of crotonaldehyde exiting the reactor, determined through online GC analysis, divided by the total mass of the catalyst. Crotonaldehyde may be consumed through further condensation reactions, however, production of higher order condensation products was small (<20% of GC product area) for the differential conversions used in this study (<10%). All reaction rates discussed in the following sections of this study represent net reaction rates.

Turnover frequencies (TOFs) were calculated using the rate of crotonaldehyde production on the Al_2O_3-supported catalysts after 10 h on stream at 300°C. These values represent an average TOF across the length of the catalyst bed. The number of active sites was estimated as the mass-normalized number of medium + strong acid sites present on each catalyst, as determined through pyridine FTIR experiments. The TOF was then calculated by dividing the overall reaction rate by the total number of medium + strong acid sites for each catalyst.

Temperature programmed oxidation. Spent catalyst samples were generated using the same conditions listed above for aldol condensation reaction testing (10 h on stream at 300 °C). Samples were then loaded into a separate reactor system with downstream Pfeiffer Prisma quadrupole mass spectrometer for analysis. Samples were purged in a stream of 1 sccm O_2 and 20 sccm He at room temperature for 30 minutes before the temperature was ramped to 700 °C at 10 °C/min. The quantity and reactivity of carbonaceous deposits on each sample were compared by analyzing signals associated with the desorption of CO (m/z = 28) and CO_2 (m/z = 44).

Thermogravimetric analysis. A small aliquot of the spent sample (~20 mg) was loaded into a thermogravimetric analyzer (TGA, SDT-Q600 by TA) to quantify the carbonaceous deposition. The sample was stabilized at 30 °C for 10 min in 50 sccm of air to desorb potential physisorbed water. Then, the temperature was ramped to 750 °C at 10 °C min^{-1}. That temperature was held for 60 min.

Infrared spectroscopy for spent catalysts. Attenuated total reflectance infrared spectroscopy (ATR-FTIR) was used to identify the moieties comprising the carbonaceous species on the catalyst. The IR spectra were recorded without any pretreatment, at room temperature using a Thermo Fisher Scientific Nicolet iS20 instrument equipped with a Smart iTR ATR sampling accessory with a single-reflection ZnSe crystal. The resolution used was 4 cm^{-1}, and 64 scans were recorded. The instrument was equipped with an MCT/A detector cooled at the liquid nitrogen temperature (-196 °C).

N_2 physisorption. The nitrogen physisorption isotherms were measured at the liquid nitrogen temperature (-196 °C) using a Micromeritics ASAP 2020 physisorption analyzer. The catalysts were degassed at 200 °C for 4 h before measurement. The surface area and mesopore volume for each sample were calculated by using the BET method and BJH method, respectively.[35,36] Samples were run twice each.

Electron microscopy. The powder sample was dispersed in ethanol, then dropped on holy carbon coated Cu grids after being ultrasonicated for 5 minutes. A Hitachi HD2700 aberration-corrected scanning transmission electron microscope was used to record the high-angle annular dark-field (HAADF) STEM images. The electron beam convergent angle α was 27 mrad and the HAADF detector collection angle β=70–370 mrad.

Ultraviolet-visible diffuse reflectance spectroscopy. A Harrick Praying Mantis diffuse reflectance setup with high temperature reactor was used in tandem with ThermoFisher Evolution 300 UV/VIS spectrophotometer. Barium sulfate was used as the 100% transmittance baseline. γ-Al_2O_3 was dehydrated at 450 °C for 1 h before being brought down to room temperature for measurement. The signal from γ-Al_2O_3 was subtracted from the signals obtained for the supported catalysts. Each sample was first calcined in air and brought down to room temperature before reduction under the same temperature program. Spectra were treated with the Kubelka-Munk remission. Tauc plots were generated using the ligand to metal charge transfer (LMCT) peaks at 237 nm and 320 nm. Linear regions of the plot were fitted with a line of best fit where the x-intercept was taken as the bandgap value. The Tauc method was used to determine bandgap values as described elsewhere.[37]

X-ray absorption near edge spectroscopy (XANES). XANES was performed on beamline 9-3 at the Stanford Synchrotron Radiation Laboratory (SSRL) to determine the effect of H_2 treatment on the oxidation state of a 10Mo/Al_2O_3 sample. Experiments were performed at the Mo K-edge, and all energies were calibrated in reference to a Mo foil standard that was collected during each run and defined as 20000 eV. Edge energies were calculated as the maximum of the 1st derivative. Powder catalyst samples were packed into a capillary flow tube for in-situ analysis during reduction. XAS spectra were collected continually while the reactor tube was purged at room temperature in He for 10 min before ramping to 450 °C at 10 °C/min and being held at this temperature for 1 h. XANES spectra were processed and analyzed using Athena.[38]

Temperature programmed desorption. In each experiment, about 100 mg of 10Mo/Al_2O_3 was loaded into a quartz reactor tube between two layers of quartz wool. The sample was then pretreated in 36 sccm of either H_2 or O_2 at 450 °C for 1 hour and then purged in 36 sccm He at 450 °C for 30 minutes before being cooled down to room temperature. Samples were dosed using a stream of 9 sccm He passing through a Pyrex bubbler tube filled with 20 mL of acetaldehyde held at 1 °C and then over the catalyst bed for 30 min. Following dosing, samples were purged in 9 sccm He for approximately 8 hours at room temperature. Subsequently, samples were heated from room temperature to 700 °C at a rate of 10 °C/min. Desorption products were detected with a Pfeiffer Prisma quadrupole mass spectrometer downstream of the reactor.

Post-Reaction Catalyst Capacity Measurements. Samples of about 100 mg of 10Mo/Al_2O_3 were loaded into a quartz reactor tube between two layers of quartz wool before being treated in 36 sccm of H_2 at 450 °C for 1 h and then purged in 36 sccm He for 30 min. Some samples were then exposed to the same reaction conditions used for catalyst evaluation (300 °C, $P_{acetaldehyde}$ = 0.07 atm, WHSV = 1.4 h^{-1}) for varying periods of time before purging in He at 300 °C for 15 min and cooling down to room temperature. The number of active sites available after reaction was quantified by subsequently dosing the catalyst with either acetaldehyde or pyridine. Samples were dosed with a stream of 9 sccm He passing through a Pyrex bubbler tube containing the desired probe molecule (acetaldehyde held at 1 °C, pyridine held at room temperature) for 30 minutes. Samples were then allowed to purge for approximately 8 hours at room temperature before being heated at a rate of 10 °C/min to 700 °C. Subsequently, samples that had been exposed to acetaldehyde reaction conditions were subjected to a temperature programmed oxidation cycle.

3. Results

3.1 Activity and Stability of Supported Catalysts

The performance of Al_2O_3 and SiO_2 supported Mo catalysts with different Mo loadings was analyzed for the steady-state aldol condensation of acetaldehyde to crotonaldehyde. Rates of crotonaldehyde production after H_2 pretreatment and 10 hours on stream are shown in Figure 1A. Plots of conversion and crotonaldehyde yield for the same experiments are displayed in Figure S2. Complex product mixtures were produced over all catalysts, including small amounts of various C_4-C_8 condensation products (e.g., 2,4-hexadienal, 2-methyl-2-cyclopenten-1-one, and 2-methylbenzaldehyde) as well as light hydrocarbons from cracking reactions, but the selectivity to crotonaldehyde was high for all catalysts (>80% of GC FID product area) at the low conversions studied here (<10%). Approximate molar carbon selectivities for each identified reaction product (as determined through GC peak area), including higher order condensation products, are displayed for all catalyst samples in Table S1. Although crotonaldehyde underwent further condensation to higher products, the direct aldol condensation of acetaldehyde is the focus of this study and crotonaldehyde can be thought of as an intermediate within a larger reaction network. The presence of Mo generally increased the activity compared to the bare γ-Al_2O_3 and SiO_2 supports, but the optimal weight loading varied. An important distinction is the fact that the bare γ-Al_2O_3 support showed significant activity for the condensation reaction, whereas the bare SiO_2 support did not. As a result, the addition of Mo to Al_2O_3 provided enhancement to an already active catalyst. On the γ-Al_2O_3 support, the samples with the lowest Mo loading (1Mo/Al_2O_3) exhibited the highest overall activity and catalytic efficiency per Mo site. The activity appeared to decline with increasing Mo loading, with the highest Mo loading sample (20Mo/Al_2O_3) demonstrating similar activity to the bare γ-Al_2O_3 support. On the SiO_2 support, the activity of the catalysts increased monotonically with increasing Mo loading up to 10 wt.%. The trend in activity for the Mo/SiO_2 samples appeared to approach the activity of the Mo/Al_2O_3 samples, particularly when extrapolated to high Mo loadings. This suggests that at very high weight loadings, the activity of the catalyst is dominated by the MoO_x phase, and the interactions between catalyst and support become less important. When normalizing production of crotonaldehyde by mass of Mo rather than total catalyst mass (Figure S2), the SiO_2 supported samples displayed similar reaction rates regardless of the Mo loading. Interestingly, on the γ-Al_2O_3 support, the low loading 1Mo/Al_2O_3 catalyst demonstrated higher Mo-normalized activity than any of the other samples. The difference in activity between the 10Mo/Al_2O_3 and 10Mo/SiO_2 samples can be primarily attributed to the additional activity of the Al_2O_3 support, as evidenced by the similar Mo normalized rates for these two samples (Figure S2).

Each sample exhibited deactivation over the course of the 10 hours on stream, which can potentially be attributed to a variety of chemical, mechanical, and thermal degradation pathways.[39] One potential means of deactivation for the aldol condensation reaction is site poisoning through the build-up of strongly-bound carbonaceous species over the course of the reaction. This hypothesis was tested by examining the activity of a 10Mo/Al_2O_3 sample for the aldol condensation of acetaldehyde while performing oxidation-reduction regeneration cycles at regular 3 h intervals (Figure 1B). Each regeneration cycle restored the conversion of the sample, and the deactivation profiles between each cycle appeared to be nearly identical. When a similar experiment was carried out on another 10Mo/Al_2O_3 sample using reduction-only regeneration cycles, the activity of the sample was not fully regenerated after each cycle (Figure S3). This result implies that some activity can be recovered through thermal desorption and reduction cycles, but an oxidizing environment is needed to fully remove carbonaceous deposits and completely regenerate the initial state of the catalyst surface.

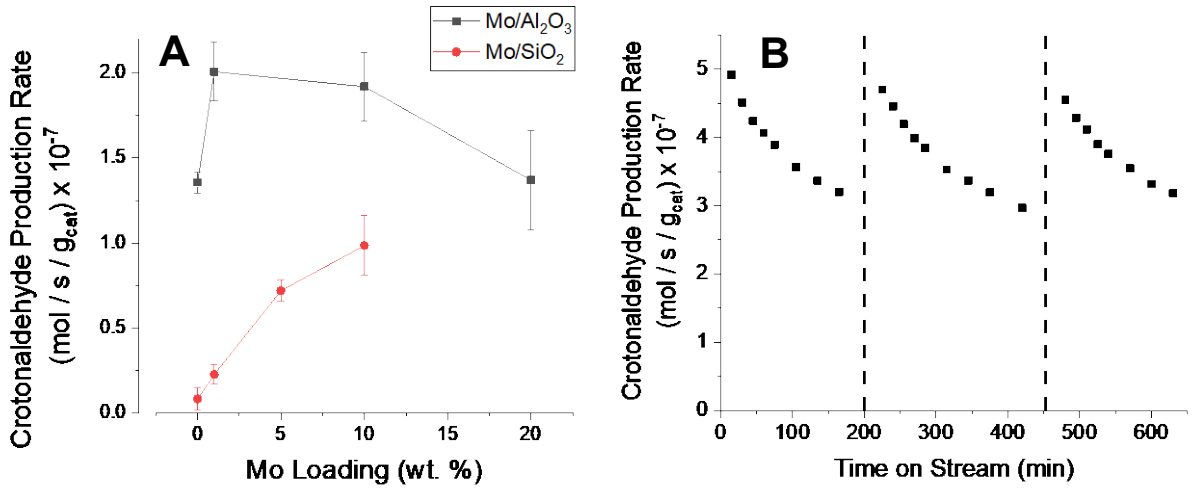

Figure 1: Summary of supported Mo catalyst performance. Mass-normalized crotonaldehyde formation rate is plotted as a function of Mo loading (A) during the steady state reaction of acetaldehyde on various Mo-modified catalysts at WHSV = 1.4 hr^{-1} after pretreatment in 36 sccm H_2 at 350 °C for one hour and 10 hours reaction at 300 °C. Crotonaldehyde production rate plotted as a function of time on stream (B) for the aldol condensation of acetaldehyde at 300 °C on a $1Mo/Al_2O_3$ catalyst after pretreatment in H_2 at 350 °C for 1 h. Dotted lines represent regeneration cycles, which involved treatment in O_2 at 350°C for 30 min followed by H_2 at 350 °C for 30 min.

Carbonaceous build-up during reaction was characterized by measuring CO_2 (m/z = 44) evolution during TPO (Figure S4). The areas underneath the desorption profiles associated with both CO and CO_2 were calculated and used to compare the total amount of carbonaceous deposits on each catalyst (Table S2). Bare SiO_2 showed very little build-up compared to the Al_2O_3 and $10Mo/Al_2O_3$ samples. However, modification of SiO_2 with Mo dramatically increased the amount of CO_2 produced during TPO. Overall, the amount of CO_2 produced by each sample during TPO appears to be correlated to the activity of the catalysts. This may suggest that both the density and efficiency of the active sites are intrinsically linked to the deactivation profile for a given catalyst. The SiO_2 and $10Mo/SiO_2$ samples also exhibited small CO_2 desorption peaks at low temperatures, which have been attributed to physisorbed CO_2. A prior study by Ueno and Bennett found that CO_2 physisorbed on SiO_2 would desorb at temperatures as low as 31°C, which is consistent with the low desorption temperatures observed in this study.[40] The wide peak shape for CO_2 production on Al_2O_3 may be caused by the presence of at least two different surface sites. Similarly broad, high-temperature peaks for CO_2 production have been observed previously during TPOs of acetaldehyde on bare Al_2O_3.[41]

The carbonaceous buildup was also evaluated and quantified by TGA of spent catalyst samples (Figure S5). The derivative of the weight profile was found to be in good agreement with the profiles obtained during TPO experiments reported in Figure S4. The carbonaceous deposits were quantified to be 4.4 wt%, 8.6 wt%, 5.9 wt% and 7.9 wt% for SiO_2, Al_2O_3, $10Mo/SiO_2$ and $10Mo/Al_2O_3$, respectively. The last mass drop at 730 °C for $10Mo/SiO_2$ was attributed to MoO_3 sublimation and as such not considered in the quantification of carbonaceous deposits.[42] Additionally, the composition of the carbonaceous deposits was characterized by ATR-FTIR spectroscopy (Figure S6). Bands at 1715 and 1668 cm^{-1} were detected for surface species on the $10Mo/SiO_2$ and were attributed to C=O vibrations of acetaldehyde and crotonaldehyde, respectively.[19,43] The band at 1668 cm^{-1} was not observed on SiO_2, while a shoulder at

1758 cm^{-1} was detected and attributed to a C=O mode of some condensation product.[44] The surface species observed on Al_2O_3 and 10Mo/Al_2O_3 were different from the ones observed on the SiO_2 supported samples. The two broad features at 1573 and 1450 cm^{-1} were attributed to acetates probably formed by the Tishchenko reaction.[45,46] Additionally a small shoulder at 1705 cm^{-1} could be related with the presence of acetaldehyde.[19,43]

The differences in activity trends for γ-Al_2O_3 and SiO_2 supported catalysts suggested that MoO_x-support interactions played an important role in the efficiency of the active site for the aldol condensation reaction. To better understand this phenomenon, a variety of characterization techniques were performed on these samples, and the results were compared to trends in catalyst activity.

3.2 Catalyst Structure Characterization

Catalyst surface area and pore volumes were determined through N_2 physisorption (Table 1). The bare SiO_2 support had the highest surface area, and deposition of Mo onto the SiO_2 surface at 10 wt% reduced this surface area to roughly half of that of the bare support. As weight loading of MoO_x increased on SiO_2, there was a monotonic decrease in surface area, likely due to crystalline MoO_x domains covering the amorphous SiO_2 support via filling of the pores. A similar, large reduction in surface area due to Mo deposition on silica has been shown in other studies.[47,48] On γ-Al_2O_3, the surface area remained roughly the same for all samples with a slight increase for 1Mo/Al_2O_3. The 20Mo/Al_2O_3 sample had both the lowest surface area and pore volume suggesting pore blockage of the Al_2O_3 support was occurring. Chakrabarti and Wachs report that 4.6 Mo atoms/nm^2 is the density corresponding to monolayer coverage of MoO_x on Al_2O_3.[49] Thus, both the 10 and 20Mo/Al_2O_3 samples have loadings at or greater than monolayer coverage, respectively.

Table 1: BET surface areas of γ-Al_2O_3 and SiO_2 supported Mo catalysts calculated by N_2 physisorption experiments.

Sample	BET SA (m^2/g)	Pore Volume (cm^3/g)	Mo Density (Mo atoms/nm^2)
SiO_2	338 ± 3	0.953 ± 0.007	-
1Mo/SiO_2	310 ± 2	0.931 ± 0.001	0.20
5Mo/SiO_2	275 ± 1	0.86 ± 0.03	1.1
10Mo/SiO_2	147 ± 2	0.77 ± 0.01	4.3
Al_2O_3	113 ± 1	0.31 ± 0.01	-
1Mo/Al_2O_3	135 ± 3	0.313 ± 0.002	0.46
10Mo/Al_2O_3	117 ± 5	0.28 ± 0.03	5.4

20Mo/Al_2O_3	**97 ± 1**	**0.185 ± 0.001**	**12.9**

The MoO_x particle sizes for 10Mo/SiO_2 and γ-Al_2O_3 supported materials were determined using TEM imaging (Figure S7). Table 2 shows that the feature sizes of MoO_x species increased with increasing loading on the γ-Al_2O_3 support. Particle size distributions of Mo domains in selected samples are shown in Figure S8.

Table 2. Average particle size of MoO_x species based on TEM images.

Material	Particle Size (nm)
1Mo/Al_2O_3	0.8 ± 0.1
10Mo/Al_2O_3	1.2 ± 0.2
20Mo/Al_2O_3	1.5 ± 0.3

The effect of weight loading on the formation of catalytic sites was further investigated with UV-VIS diffuse reflectance spectroscopy to determine bandgaps for Mo/Al_2O_3 (Figure 2). As shown by Chakrabarti and Wachs, lower bandgap values of Mo supported on γ-Al_2O_3 indicate larger molybdenum clusters (> 1 nm) on the surface, and higher bandgaps translate to smaller dimeric and monomeric (< 1 nm) MoO_x species on the support.[49] A broad feature at 320 nm is assigned to polymeric MoO_x while 245 nm is attributed to oligomeric MoO_x species. At lower loadings, the isolated, oligomeric species dominated while at higher loadings there was more polymeric species in addition to oligomeric MoO_x. As weight loading was increased, the bandgap fell, due to larger oxide clusters forming as also shown from Table 2. The bandgap for a bulk MoO_3 sample from Sigma Aldrich (99.99% trace metal basis) was measured as 2.1 eV, significantly lower than the 3.5 eV bandgap measured for the 20Mo/Al_2O_3 sampleInterestingly, the reductive pretreatment also decreased the bandgap for all MoO_x-containing samples, suggesting that high temperature H_2 treatments are able to significantly influence the oxidation state of Mo for each catalyst. These bandgap measurements also support the findings from the XANES analysis (Figure 5A), where the oxidation state of Mo in the 10Mo/Al_2O_3 sample was found to decrease from 6 to approximately 3.2 when the sample was heated to 450 °C in H_2. The difference due to reduction was more pronounced at higher weight loadings because molybdenum oxide reducibility depends strongly on the oxide structure.[25]

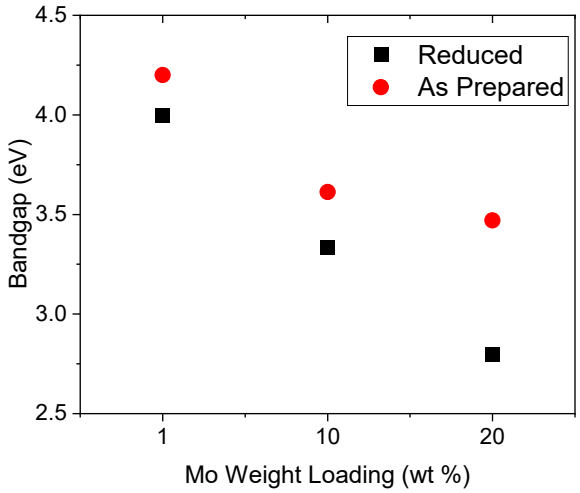

Figure 2. Bandgaps of different weight loadings of Mo/Al_2O_3 after reduction and as prepared after calcination.

3.3 Acid Site Characterization

To understand how the activity trends with respect to Mo loading shown in Figure 1 relate to the density and properties of surface acid sites, we characterized the catalysts using pyridine adsorption followed by FTIR spectroscopy (Figure 3). The concentrations of Lewis and Brønsted acid sites were measured before (Figure 3a, b) and after (Figure 3c, d) reduction of the catalyst at 450 °C for 1 h in hydrogen. After reduction, the concentrations of Lewis acid sites were lower compared to the as-prepared samples for the MoO_x deposited on SiO_2 catalysts but not the γ-Al_2O_3 supported catalysts. The concentration of Lewis acid sites that retained pyridine at 450 °C was the same or higher for all γ-Al_2O_3 supported materials.

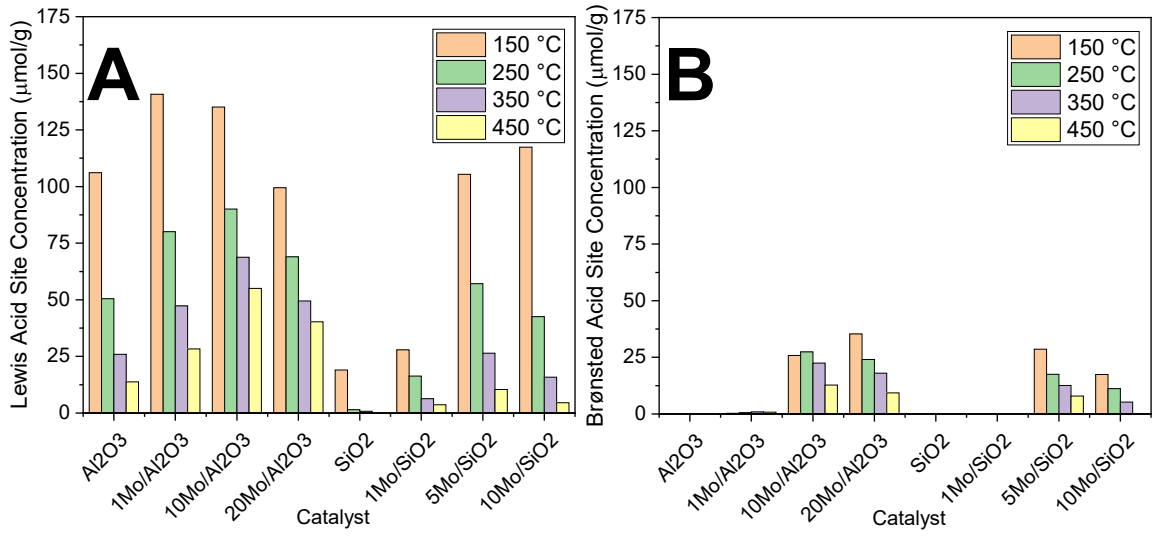

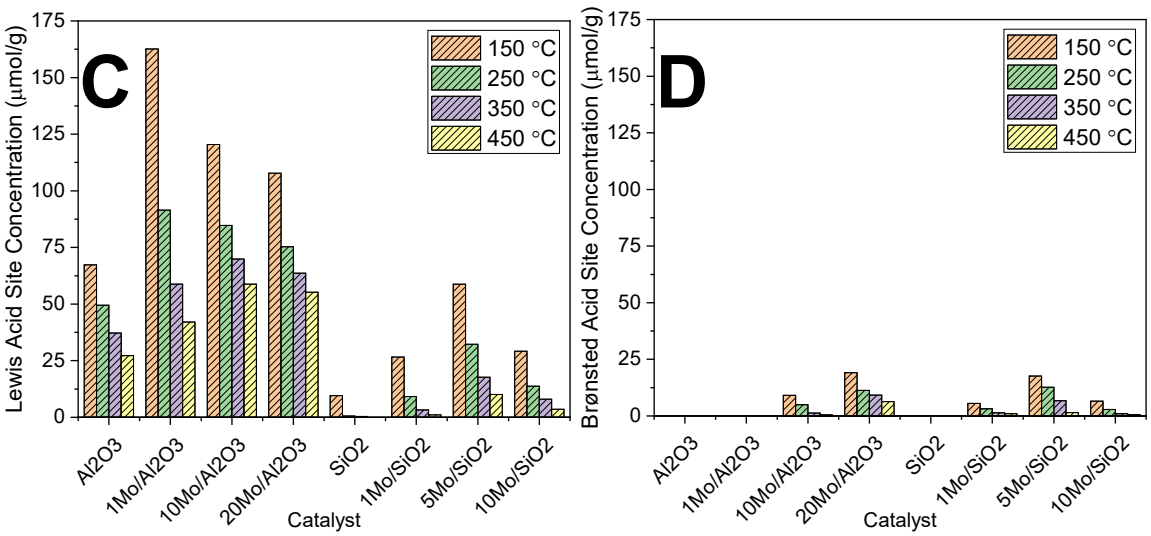

Figure 3. Lewis (A and C) and Brønsted (B and D) acid site concentration measured using pyridine transmission FTIR spectroscopy of molybdenum supported catalysts before (A and B) and after reduction (C and D).

The relative strengths of Lewis acid sites were estimated using the pyridine IR data shown in Figure 3. The density of Lewis acid sites on each catalyst was categorized into three desorption ranges (Figure 4), representing sites associated with relatively weak (150 °C - 250 °C), moderate (250 °C - 450 °C), and strong (450 °C and above) Lewis acid character. SiO_2 and $10Mo/SiO_2$ both showed a relatively high concentration of weak acid sites but contained very few if any strong Lewis acid sites. On the other hand, Al_2O_3 and $10Mo/Al_2O_3$ both contained a higher density of strong acid sites than medium or weak sites. Modification of SiO_2 and γ-Al_2O_3 with Mo produced catalysts with a higher overall density of acid sites, as well as a larger fraction of strong acid sites in both cases.

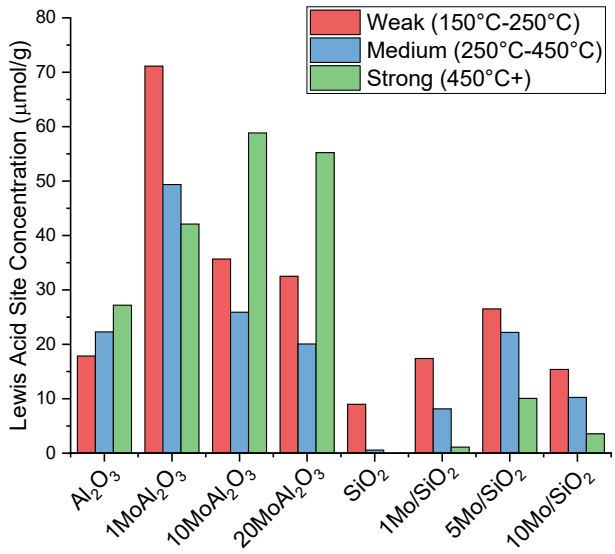

Figure 4. Density of Lewis acid sites desorbing pyridine within specific temperature ranges, calculated from data in Figure 3.

Similar trends with respect to the strength of Lewis acid sites were observed using acetonitrile-d^3 (CD_3CN) adsorption followed by FTIR spectroscopy (Figure S9). The peak associated with acetonitrile bound to LAS was found to be at a higher frequency on $10Mo/Al_2O_3$ (2320 cm^{-1}) compared to $10Mo/SiO_2$ (2310 cm^{-1}) before reduction, suggesting that the MoO_x sites on the γ-Al_2O_3 support were stronger Lewis acids (Figure S9).[34] Peaks around 2273 cm^{-1} was assigned to surface hydroxyl groups, and peaks near 2111 cm^{-1} associated with physisorbed acetonitrile were also detected.[50,51] For the reduced samples, there was a blueshift from 2320 cm^{-1} (Figure S9A) to 2323 cm^{-1} (Figure S9B) indicating stronger Lewis acidity.

3.4 Effect of Pretreatment Conditions on Supported Mo Catalysts

The role of reduced MoO_x sites in the aldol condensation reaction was probed through a variety of temperature programmed characterization techniques. XANES spectra of the Mo K-edge were collected as the sample was resistively heated in flowing H_2 gas (Figure 5A) to determine the effect of reducing conditions on the Mo oxidation state. At room temperature, the Mo K-edge structure for the $10Mo/Al_2O_3$ sample closely resembled the MoO_3 standard. As the sample was heated, the pre-edge shoulder began to disappear, and the K-edge shifted to lower energies, indicating that reduction was occurring.

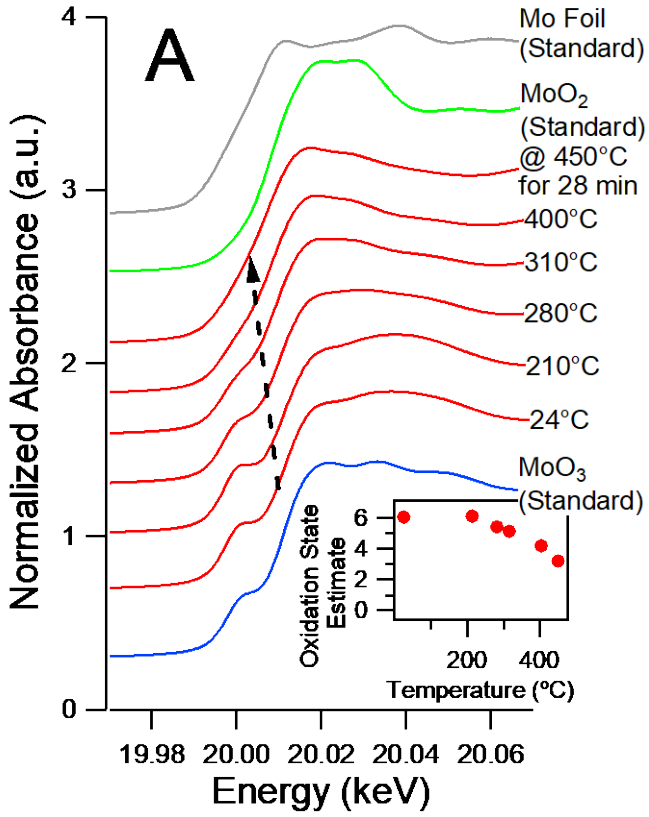

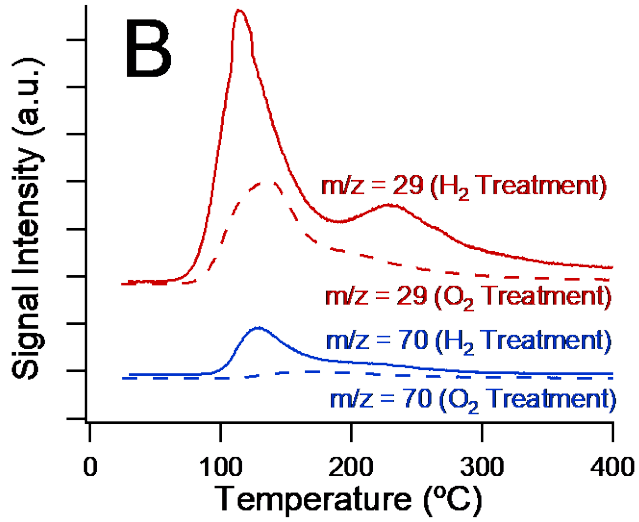

Figure 5. XANES spectra (A) and acetaldehyde TPD (B) characterization of the effect of H_2 pretreatments on $10Mo/Al_2O_3$. Mo K edge XANES spectra (A) collected during a temperature ramp in pure H_2 flow. Mo K edge XANES spectra of Mo foil, MoO_2, and MoO_3 standards are also plotted for comparison. Dashed line shows shifts in the adsorption edge energy as the temperature is ramped. Inset: estimated oxidation state of sample as a function of temperature. TPD profiles for acetaldehyde dosed on a $10Mo/Al_2O_3$ catalyst (B) after treatment with 36 sccm H_2 or O_2 at 450 °C for one hour.

For each XANES spectrum collected, the oxidation state of the $10Mo/Al_2O_3$ sample was estimated by comparing the Mo K-edge energy to a linear fit of the K-edge energies for the Mo foil, MoO_2, and MoO_3 standards (Figure S10). The calculated oxidation state of the sample as a function of the sample temperature is shown in the inset for Figure 5A. As the sample was heated, the oxidation state steadily decreased, ultimately reaching a final value of approximately 3.2 after being held at 450 °C for several minutes. This result indicates that high temperature H_2 pretreatments are highly effective for reducing Mo clusters on supported Mo/Al_2O_3 catalysts. These reduced Mo sites may then act as Lewis acid sites for the aldol condensation reaction as discussed below.

The role of Mo reduction in the aldol condensation reaction was further probed through TPD of acetaldehyde on a $10Mo/Al_2O_3$ sample pretreated with H_2 or O_2 at high temperatures. The desorption traces for masses associated primarily with acetaldehyde (m/z = 29) and crotonaldehyde (m/z = 70) were plotted as a function of temperature (Figure 5B). Crotonaldehyde was the main reaction product with a desorption temperature around 120 °C on the H_2 treated surface. On the O_2 treated catalyst, crotonaldehyde desorption shifted to slightly higher temperatures, and the peak intensity was significantly smaller. The ratio of the peak areas associated with crotonaldehyde formation (m/z = 70) on the H_2 and O_2 treated catalyst was approximately a factor of 4 higher, indicating that more crotonaldehyde was formed after H_2 pretreatment compared to the O_2 treatment. Mass fragments associated with other reaction products were also detected (m/z = 54, m/z = 73) at higher temperatures (~230 °C), but the identity of these side products was not determined. The increased desorption signal intensity for both reactants (acetaldehyde) and products (crotonaldehyde), as well as the lower temperature for product formation, suggested that the reduced MoO_x clusters on the surface of the catalyst were able to bind and activate more acetaldehyde for the aldol condensation reaction.

The effect of pretreatment conditions on the aldol condensation reaction was also analyzed using a packed bed reactor with continuous acetaldehyde feed under steady state conditions. A comparison of the rates of crotonaldehyde production after pretreatment with H_2 or O_2 and 10 hours of reaction on stream at 300 °C is shown in Figure S11. Unlike the TPD results, the steady state reactor data showed no significant difference in aldol condensation activity between the two pretreatments. This suggests that acetaldehyde can also participate in redox reactions with the catalysts, so that the surface structure of the catalysts may equilibrate at an oxidation state that is primarily determined by the reaction conditions, rather than the pretreatment conditions.

Successive reaction and TPD experiments were conducted on samples of $10Mo/Al_2O_3$ to better understand the effect of the aldol condensation reaction on catalyst capacity and surface structure. Initially samples were pretreated in H_2 and then subjected to aldol condensation reaction conditions at 300 °C for varying periods of time (0 min, 3 min, 3 h). These "spent" samples were then cooled to room temperature and exposed to doses of acetaldehyde (Figure S12A, S12B) or pyridine (Figure S12D) before undergoing TPD analysis.

TPDs of acetaldehyde on spent samples showed dramatically reduced desorption of both acetaldehyde (Figure S12A) and crotonaldehyde (Figure S12B) after 3 min of reaction. Desorption signals continued to decrease only very slightly after 3 hours of reaction. These results suggest that the overall capacity of the catalyst for acetaldehyde adsorption and reaction is greatly decreased during the first few minutes of reaction at 300 °C. This may be caused by a combination of strongly bound carbonaceous species building up on the surface and changes to the oxidation state of the MoO_x particles. Following these TPDs, the samples after 0 min and 3 min of reaction were subjected to TPOs to quantify the amount of strongly bound carbonaceous species that did not desorb during the TPD cycle (Figure S12C). Significantly more CO_2 formation was observed for the spent sample after 3 min of aldol condensation reaction at 300 °C compared to 0 min, indicating that strongly bound carbonaceous species are rapidly built up on the catalyst surface during the first few minutes of reaction. This result also supports the finding that the overall catalyst capacity is dramatically reduced after only 3 minutes of aldol condensation reaction.

TPDs of pyridine on spent samples (Figure S12D) were utilized to quantify the effect of the aldol condensation reaction on the density of available acid sites. Similar trends were observed to the acetaldehyde TPD experiments, where the pyridine desorption signal decreased dramatically after the first 3 minutes of aldol condensation reaction and further decreased after 3 hours of time on stream.

4. Discussion

Molybdenum oxide (MoO_x) based catalysts have been shown to effectively catalyze various reactions such as olefin metathesis, ethane dehydrogenation and lignin hydrogenolysis.[24,52,53] The active MoO_x phase in these catalysts is typically deposited on high surface area supports due to the low surface area of bulk molybdenum oxides.[54] For many of these reactions, the active phase of MoO_x is a partially reduced Mo center, and as such, the supported MoO_x catalysts are typically activated through reductive pretreatments or reaction conditions. We have previously shown that the reduction of bulk MoO_3 to a lower oxidation state facilitated greater adsorption of ethanol and acetaldehyde and activated these molecules for the aldol condensation reaction.[22] This effect was attributed to the creation of

coordinatively unsaturated sites on the MoO_x surface via oxygen vacancies which can then activate oxygen-containing compounds for the aldol reaction. In this study, we deposited MoO_x on high surface area oxides (SiO_2 and γ-Al_2O_3) and pretreated them under different gases (H_2 and O_2) to understand the role of reductive pretreatments and reaction conditions on the nature of supported MoO_x catalysts. XANES spectra of 10Mo/Al_2O_3 during heating in H_2 flow (Figure 5A) demonstrated that high temperature H_2 treatments can reduce surface Mo clusters to suboxide states. Furthermore, TPD of acetaldehyde on H_2 and O_2 treated 10Mo/Al_2O_3 samples (Figure 5B) showed that the reduced catalyst was able to adsorb and activate a greater quantity of acetaldehyde and convert these molecules via the aldol condensation reaction. These results indicate that reduced Mo sites on supported catalysts, in the form of oxygen vacancies, are able to assist in the adsorption and activation of light oxygenates, similar to what we have seen previously on bulk molybdenum oxides.[22] Similarly, Harlin et al. demonstrated that reduced Mo centers (oxidation state ~4.3) in Mo/Al_2O_3 produced during reductive pretreatments exhibited increased conversion for n-butane dehydrogenation.[26] However, in this study, steady state reactor comparisons of a 10Mo/Al_2O_3 sample showed no difference in the rate of acetaldehyde condensation to crotonaldehyde after pretreatments in H_2 or O_2 and 10 hours of reaction on stream (Figure S11). This indicates that the structure of the catalyst equilibrated under reaction conditions regardless of the pretreatment. Similarly, it has been observed for m-cresol hydrodeoxygenation using bulk MoO_3 that prereduction in H_2 has a larger effect on the initial induction period rather than the steady state conversion.[55] Post-reaction TPD experiments demonstrated that the overall catalyst capacity changes dramatically during the first few minutes of reaction (Figure S12). Carbonaceous species build up rapidly on the surface of the catalyst and the number of available acid sites drops significantly (Figure S12D), thereby indicating that changes in surface structure occur quickly under high temperature aldol condensation conditions. Additionally, the aldol condensation reaction evolves water, which may be involved in transforming the catalyst surface structure after multiple turnovers. As a result, while pretreatment conditions may have a significant impact on the initial reactivity of the catalyst surface, we hypothesize that the reaction process conditions govern the redox state and ultimately the activity of the catalyst under steady-state conditions.

Numerous observations from this study indicate that the interactions between Mo and γ-Al_2O_3 are stronger than those between Mo and SiO_2. On the γ-Al_2O_3 support, as weight loading increased, the average particle size also increased (Table 2). A comparison of the structure of these materials has previously shown that crystallization of Mo oxides and poor dispersion occurs on SiO_2 due to weaker Mo-support interactions during impregnation.[56] In contrast, Chakrabarti and Wachs demonstrated that MoO_x supported on Al_2O_3 was anchored as isolated and oligomeric species on basic and surface hydroxyl (OH) sites of the Al_2O_3 support.[49]

We observed that the relationship between Mo weight loading and aldol condensation rate on γ-Al_2O_3-supported materials exhibited a maximum at relatively low Mo loading (1Mo/Al_2O_3). The concentration of LAS on the 1Mo/Al_2O_3 sample was also higher compared to samples with higher weight loadings (Figure 3). Thus, highly dispersed oligomeric MoO_x particles seen at low weight loadings are more acidic and contain a higher density of active sites than larger MoO_x agglomerates. Mo loading can also affect the steric accessibility of the active site. Prior characterization studies of MoO_3/Al_2O_3 catalysts have shown that the coordination environment of Mo tends to change with MoO_x loading. At low MoO_x loadings, the primary Mo surface configuration has been identified as a tetrahedrally coordinated, isolated dioxo $(O=)_2MoO_2$ species. As the weight loading increases, a higher fraction of oligomeric mono-oxo $O=MoO_4$ species are present, and at high loadings the surface is dominated by crystalline MoO_3 in a

distorted octahedral structure.[49,57,58] Both isolated and oligomeric MoO_x species were observed at low and high loadings, as indicated by the bandgaps reported in Figure 2. In general, Mo coordination tends to increase with increasing weight loading, from tetrahedral species at low loadings to octahedral crystals at very high loadings. As a result, the Lewis acidic, cationic Mo active site is more accessible (relative to bulk MoO_3) at low loadings, thereby facilitating the accessibility of carbonyl adsorption and ultimately resulting in a higher rate of acetaldehyde condensation.

A key difference between the γ-Al_2O_3- and SiO_2-supported samples is the Lewis acidity of the support. Since SiO_2 does not possess Lewis acidity (Figure 3), increasing MoO_x loading does not block any preexisting active sites. In contrast, the γ-Al_2O_3 support already contains significant Lewis acidity, so blocking Al active sites with MoO_x species would be expected to decrease rates, unless the new MoO_x sites are more efficient for aldol condensation than the bare Al_2O_3. Due to this effect, increasing the MoO_x loading generally tends to drive the conversion on a SiO_2 support up and the conversion on an Al_2O_3 support down (Figure 1A). At very high MoO_x loadings we expect that both supports will approach a similar conversion as the surface becomes completely covered by layers of MoO_x, and the interaction with the support becomes less important. When production of crotonaldehyde was normalized to the mass of Mo (Figure S2), the 1Mo/Al_2O_3 sample exhibited a much higher value compared to all other samples, but this observation did not account for the existing active sites on bare Al_2O_3. The addition of Mo can therefore be thought of as an enhancement to an already active catalyst to an extent. As seen with 20Mo/Al_2O_3, there is more than monolayer coverage of MoO_x on the surface and the production of crotonaldehyde is roughly the same as bare Al_2O_3. This suggests an optimal for MoO_x loading on Al_2O_3 is needed to observe enhanced performance.

Acid site strength was considered as a descriptor for aldol condensation on metal oxide catalysts. Several factors previously discussed may influence this Lewis acid strength, such as the geometry of the MoO_x particles, the particle size, the oxidation state under reaction conditions, and interactions with the support. Saraeian et al. demonstrated using NH_3-TPD that as the weight loading of MoO_x increased on an Al_2O_3 support, the concentration of strong acid sites decreased and pore blockage of the Al_2O_3 support occurred. We hypothesize that at higher MoO_x loadings, pore blockage of γ-Al_2O_3 results in a loss of strong acid sites and ultimately causes the drop in crotonaldehyde production between 10Mo/Al_2O_3 and 20Mo/Al_2O_3. In the present study, we compared the acetaldehyde steady state aldol condensation activity of a variety of supported Mo catalysts (Figure 1A) to their relative acid site strength and density as measured by pyridine FTIR (Figure 4). We then tested the correlations between the density of weak (Figure S13A), medium (Figure S13B), strong (Figure S13C), and medium + strong (Figure 6) acid sites on each catalyst to their crotonaldehyde production rate. All correlations exhibited fairly low P-values, indicating significant linear correlations. However, the weak Lewis acid sites displayed the weakest correlation, giving the highest P-value and the lowest R^2 value, potentially indicating that weak sites are generally unable to activate carbonyls for aldol addition. Medium, strong, and medium + strong acid sites all demonstrated strong correlations to the crotonaldehyde formation rate, but a linear regression analysis assigned the highest adjusted R^2 value to the medium + strong acid sites combined (Figure 6). Assuming medium and strong acid sites are the primary active sites for the aldol reaction, the turnover frequency (TOF) for the production of crotonaldehyde over γ-Al_2O_3-supported samples was calculated to be 2.3±0.4 $x10^{-3}$ s^{-1}. This value is similar to the TOFs reported by Rekoske and Barteau for the consumption of acetaldehyde over anatase TiO_2[60] and Flaherty and coworkers for the production of C_{4+} products from acetaldehyde/ethanol mixtures over anatase TiO_2,[18] albeit with some differences in reaction conditions.

Based on these results, we conclude that Lewis acid site strength is essential for predicting catalyst performance in the aldol condensation reaction, and acid sites of at least moderate acid strength are needed to activate acetaldehyde for this reaction.

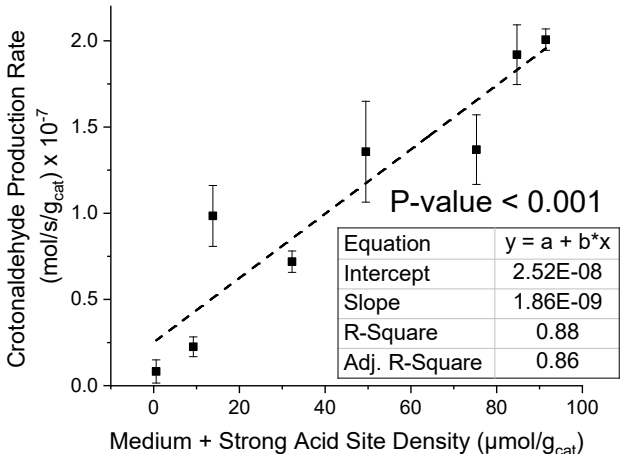

Figure 6. Crotonaldehyde production rate from acetaldehyde plotted as a function of medium + strong acid site density for a series of Mo/Al_2O_3 and Mo/SiO_2 catalysts. The calculated P-value and R^2 value for a linear correlation between these two variables are displayed on the chart.

Coking and deactivation during reaction can be influenced by a variety of different factors, including microporosity, high temperatures and high hydrocarbon pressure.[61] We propose that high concentration of strong Lewis acidic sites is the main factor responsible for the deactivation of our samples. Catalysts with a high density of Lewis acid active sites tend to have higher conversions, but the increased coverage of reactive intermediates on the surface may also increase the probability for coupling reactions that create heavier oxygenates that block active sites. For example, the $10Mo/Al_2O_3$ sample had a higher density of medium and strong LAS than $10Mo/SiO_2$ as evidenced by pyridine adsorption measurements (Figures 3 and 4), and subsequently, the spent catalyst sample displayed a larger CO_2 desorption peak at a higher temperature during TPO (Figure S4). This result suggests that a tradeoff exists between high conversion and resistance to carbonaceous buildup. Deactivation profiles for the samples displayed in Figure S1B were replotted in Figure S14 to better understand how different samples may deactivate differently. In Figure S14, the crotonaldehyde production rate is normalized by the number of medium + strong acid sites (Figure 4) and plotted on the y-axis. The total cumulative moles of crotonaldehyde produced is plotted on the x-axis. Based on this analysis, it appears that the deactivation varies to some extent across the samples, but not in a way that is clearly related to initial activity or acid site strength. However, some samples with lower initial site-normalized production rates, particularly some of the SiO_2-based samples, appeared to deactivate after fewer moles produced. Overall, our results demonstrate that catalysts with a high density of LAS (Figure 3) tend to build up significant coke deposits (Figure S4) and deactivate substantially over the course of the reaction (Figure S1B). However, these effects can be mitigated through regular oxidation-reduction cycles (Figure 1B).

5. Conclusion

Both γ-Al_2O_3- and SiO_2-supported MoO_x catalysts are active for aldol condensation of acetaldehyde to crotonaldehyde, but interactions between MoO_x and the SiO_2 and γ-Al_2O_3 supports used in this study are fundamentally different. Dispersion of MoO_x is higher and more uniform on the γ-Al_2O_3

support than the SiO_2 support due to a stronger MoO_x-support interaction. Trends in catalytic activity are also qualitatively different for the SiO_2 and γ-Al_2O_3 supported catalysts. For Al_2O_3-catalysts, the activity is highest at low Mo loadings, indicating significant beneficial particle-support interactions. As the MoO_x loading increased, the aldol condensation activity decreased toward the activity of the bare Al_2O_3 support. On SiO_2, however, the activity increased monotonically with Mo loading, indicating minimal support-particle interactions. Linear regression analysis of aldol condensation activity and pyridine FTIR revealed that the density of medium/strong acid sites were highly correlated with the rate of crotonaldehyde formation from acetaldehyde. The redox state of MoO_x significantly influenced the barriers and yields for aldol condensation of acetaldehyde during temperature-programmed studies, with more reduced Mo sites leading to much higher aldol condensation activities. However, under steady-state conditions, the redox character of supported MoO_x catalysts appeared to be controlled primarily by the reaction conditions, since use of oxidative versus reducing pretreatments had no measurable effect on activity.

6. Acknowledgements

Financial support from the National Science Foundation (grant numbers: CBET-1705444/1705500) is gratefully acknowledged. S.N. is supported by the National Science Foundation Graduate Research Fellowship under Grant No. DGE-1650044. Use of the Stanford Synchrotron Radiation Lightsource, SLAC National Accelerator Laboratory, is supported by the U.S. Department of Energy, Office of Science, Office of Basic Energy Sciences under Contract No. DE-AC02-76SF00515. We acknowledge support from Simon R. Bare and Co-ACCESS. Co-ACCESS, is supported by the U.S. Department of Energy, Office of Basic Energy Sciences, Chemical Sciences, Geosciences and Biosciences Division. We thank Dr. Yong Ding for his help with TEM and EDS imaging.

7. References

(1) McGlade, C.; Ekins, P. The Geographical Distribution of Fossil Fuels Unused When Limiting Global Warming to 2°C. *Nature* **2015**, *517* (7533), 187–190. https://doi.org/10.1038/nature14016.

(2) Huber, G. W.; Iborra, S.; Corma, A. Synthesis of Transportation Fuels from Biomass: Chemistry, Catalysts, and Engineering. *Chem. Rev.* **2006**, *106* (9), 4044–4098. https://doi.org/10.1021/cr068360d.

(3) Salvi, B. L.; Subramanian, K. A.; Panwar, N. L. Alternative Fuels for Transportation Vehicles: A Technical Review. *Renew. Sustain. Energy Rev.* **2013**, *25*, 404–419. https://doi.org/10.1016/j.rser.2013.04.017.

(4) Onda, A.; Ochi, T.; Yanagisawa, K. Selective Hydrolysis of Cellulose into Glucose over Solid Acid Catalysts. *Green Chem.* **2008**, *10* (10), 1033–1037. https://doi.org/10.1039/b808471h.

(5) Huber, G. W.; Cortright, R. D.; Dumesic, J. A. Renewable Alkanes by Aqueous-Phase Reforming of Biomass-Derived Oxygenates. *Angew. Chemie* **2004**, *116* (12), 1575–1577. https://doi.org/10.1002/ange.200353050.

(6) Orazov, M.; Davis, M. E. Tandem Catalysis for the Production of Alkyl Lactates from Ketohexoses at Moderate Temperatures. *Proc. Natl. Acad. Sci.* **2015**, *112* (38), 11777–11782. https://doi.org/10.1073/pnas.1516466112.

(7) Chheda, J. N.; Dumesic, J. A. An Overview of Dehydration, Aldol-Condensation and Hydrogenation Processes for Production of Liquid Alkanes from Biomass-Derived Carbohydrates. *Catal. Today* **2007**, *123* (1–4), 59–70. https://doi.org/10.1016/j.cattod.2006.12.006.

(8) Serrano-Ruiz, J. C.; Dumesic, J. A. Catalytic Routes for the Conversion of Biomass into Liquid Hydrocarbon Transportation Fuels. *Energy Environ. Sci.* **2011**, *4* (1), 83–99. https://doi.org/10.1039/c0ee00436g.

(9) Dutta, A.; Iisa, M. K.; Talmadge, M.; Mukarakate, C.; Griffin, M. B.; Tan, E. C.; Wilson, N.; Yung, M. M.; Nimlos, M. R.; Schaidle, J. A.; Wang, H.; Thorson, M.; Hartley, D.; Klinger, J.; Cai, H. *Ex Situ Catalytic Fast Pyrolysis of Lignocellulosic Biomass to Hydrocarbon Fuels: 2019 State of Technology and Future Research*; 2020.

(10) Idriss, H.; Diagne, C.; Hindermann, J. P.; Kiennemann, A.; Barteau, M. A. Reactions of Acetaldehyde on CeO2 and CeO2-Supported Catalysts. *J. Catal.* **1995**, *155*, 219–237.

(11) Mann, A. K. P.; Wu, Z.; Calaza, F. C.; Overbury, S. H. Adsorption and Reaction of Acetaldehyde on Shape-Controlled CeO2 Nanocrystals: Elucidation of Structure-Function Relationships. *ACS Catal.* **2014**, *4* (8), 2437–2448. https://doi.org/10.1021/cs500611g.

(12) Wang, S.; Goulas, K.; Iglesia, E. Condensation and Esterification Reactions of Alkanals, Alkanones, and Alkanols on TiO2: Elementary Steps, Site Requirements, and Synergistic Effects of Bifunctional Strategies. *J. Catal.* **2016**, *340*, 302–320. https://doi.org/10.1016/j.jcat.2016.05.026.

(13) Taifan, W. E.; Bučko, T.; Baltrusaitis, J. Catalytic Conversion of Ethanol to 1,3-Butadiene on MgO: A Comprehensive Mechanism Elucidation Using DFT Calculations. *J. Catal.* **2017**, *346*, 78–91. https://doi.org/10.1016/j.jcat.2016.11.042.

(14) Di Cosimo, J. I.; Apesteguía, C. R.; Ginés, M. J. L.; Iglesia, E. Structural Requirements and Reaction Pathways in Condensation Reactions of Alcohols on MgyAlOx Catalysts. *J. Catal.* **2000**, *190* (2), 261–275. https://doi.org/10.1006/jcat.1999.2734.

(15) Kozlowski, J. T.; Davis, R. J. Sodium Modification of Zirconia Catalysts for Ethanol Coupling to 1-Butanol. *J. Energy Chem.* **2013**, *22* (1), 58–64. https://doi.org/10.1016/S2095-4956(13)60007-8.

(16) Chieregato, A.; Ochoa, J. V.; Bandinelli, C.; Fornasari, G.; Cavani, F.; Mella, M. On the Chemistry of Ethanol on Basic Oxides: Revising Mechanisms and Intermediates in the Lebedev and Guerbet Reactions. *ChemSusChem* **2015**, *8* (2), 377–388. https://doi.org/10.1002/cssc.201402632.

(17) Yee, A.; Morrison, S. J.; Idriss, H. A Study of the Reactions of Ethanol on CeO 2 and Pd / CeO 2 by Steady State Reactions , Temperature Programmed Desorption , and In Situ FT-IR. *J. Catal.* **1999**, *186*, 279–295.

(18) Zhang, H.; Ibrahim, M. Y. S.; Flaherty, D. W. Aldol Condensation among Acetaldehyde and Ethanol Reactants on TiO2: Experimental Evidence for the Kinetically Relevant Nucleophilic Attack of Enolates. *J. Catal.* **2018**, *361*, 290–302. https://doi.org/10.1016/j.jcat.2018.02.030.

(19) Rekoske, J. E.; Barteau, M. A. Competition between Acetaldehyde and Crotonaldehyde during Adsorption and Reaction on Anatase and Rutile Titanium Dioxide. *Langmuir* **1999**, *15* (6), 2061–2070. https://doi.org/10.1021/la9805140.

(20) Young, Z. D.; Hanspal, S.; Davis, R. J. Aldol Condensation of Acetaldehyde over Titania, Hydroxyapatite, and Magnesia. *ACS Catal.* **2016**, *6* (5), 3193–3202.

https://doi.org/10.1021/acscatal.6b00264.

(21) Ordomsky, V. V.; Sushkevich, V. L.; Ivanova, I. I. Study of Acetaldehyde Condensation Chemistry over Magnesia and Zirconia Supported on Silica. *J. Mol. Catal. A Chem.* **2010**, *333* (1–2), 85–93. https://doi.org/10.1016/j.molcata.2010.10.001.

(22) Najmi, S.; Rasmussen, M.; Innocenti, G.; Chang, C.; Stavitski, E.; Bare, S. R.; Medford, A. J.; Medlin, J. W.; Sievers, C. Pretreatment Effects on the Surface Chemistry of Small Oxygenates on Molybdenum Trioxide. *ACS Catal.* **2020**, *10* (15), 8187–8200. https://doi.org/10.1021/acscatal.0c01992.

(23) Tian, H.; Wachs, I. E. Molybdena Local Structural Determination in Different Environments : Aqueous Solutions , Bulk Mixed Oxides and Supported MoOx Catalysts. *J. Phys. Chem. C* **2010**, *2* (Vi), 6. https://doi.org/10.1021/jp103269w.

(24) Yao, R.; Herrera, J. E.; Chen, L.; Chin, Y. H. C. Generalized Mechanistic Framework for Ethane Dehydrogenation and Oxidative Dehydrogenation on Molybdenum Oxide Catalysts. *ACS Catal.* **2020**, *10* (12), 6952–6968. https://doi.org/10.1021/acscatal.0c01073.

(25) Cheng, E.; Notestein, J. Catalytic Dehydrogenation of Isobutane over Supported MoOx/K-Al2O3. *J. Catal.* **2021**, *397*, 212–222. https://doi.org/10.1016/j.jcat.2021.03.032.

(26) Harlin, M. E.; Backman, L. B.; Krause, A. O. I.; Jylhä, O. J. T. Activity of Molybdenum Oxide Catalyst in the Dehydrogenation of N-Butane. *J. Catal.* **1999**, *183* (2), 300–313. https://doi.org/10.1006/jcat.1999.2413.

(27) Abello, M. C.; Gomez, M. F.; Ferretti, O. Mo/γ-Al2O3 Catalysts for the Oxidative Dehydrogenation of Propane. Effect of Mo Loading. *Appl. Catal. A Gen.* **2001**, *207* (1–2), 421–431. https://doi.org/10.1016/S0926-860X(00)00680-3.

(28) Setnička, M.; Tišler, Z.; Kubička, D.; Bulánek, R. Activity of Molybdenum Oxide Catalyst Supported on Al2O3, TiO2, and SiO2 Matrix in the Oxidative Dehydrogenation of n-Butane. *Top. Catal.* **2015**, *58* (14–17), 866–876. https://doi.org/10.1007/s11244-015-0453-2.

(29) Zhao, H.; Song, H.; Chou, L.; Zhao, J.; Yang, J.; Yan, L. Insight into the Structure and Molybdenum Species in Mesoporous Molybdena-Alumina Catalysts for Isobutane Dehydrogenation. *Catal. Sci. Technol.* **2017**, *7* (15), 3258–3267. https://doi.org/10.1039/c7cy00975e.

(30) Boufaden, N.; Akkari, R.; Pawelec, B.; Fierro, J. L. G.; Said Zina, M.; Ghorbel, A. Dehydrogenation of Methylcyclohexane to Toluene over Partially Reduced Mo-SiO2 Catalysts. *Appl. Catal. A Gen.* **2015**, *502*, 329–339. https://doi.org/10.1016/j.apcata.2015.05.026.

(31) Yu, M.; Qu, W.; Xu, S.; Wang, L.; Liu, B.; Zhang, L.; Peng, J. Interfacial Stability, Electronic Property, and Surface Reactivity of α-MoO3/γ-Al2O3 Composites: DFT and DFT + U Calculations. *Comput. Mater. Sci.* **2018**, *153* (March), 217–227. https://doi.org/10.1016/j.commatsci.2018.06.046.

(32) Handzlik, J.; Ogonowski, J. Structure of Isolated Molybdenum(VI) and Molybdenum(IV) Oxide Species on Silica: Periodic and Cluster DFT Studies. *J. Phys. Chem. C* **2012**, *116* (9), 5571–5584. https://doi.org/10.1021/jp207385h.

(33) Kozlowski, J. T.; Davis, R. J. Heterogeneous Catalysts for the Guerbet Coupling of Alcohols. *ACS Catal.* **2013**, *3* (7), 1588–1600. https://doi.org/10.1021/cs400292f.

(34) Tamura, M.; Shimizu, K.; Satsuma, A. General Comprehensive IR Study on Acid / Base Properties of Metal Oxides. *Appl. Catal. A Gen.* **2012**, *433–434*, 135–145. https://doi.org/10.1016/j.apcata.2012.05.008.

(35) Brunauer, S.; Emmett, P. H.; Teller, E. Adsorption of Gases in Multimolecular Layers. *J. Am. Chem. Soc.* **1938**, *60* (2), 309–319. https://doi.org/10.1021/ja01269a023.

(36) Barrett, E. P.; Joyner, L. G.; Halenda, P. P. The Determination of Pore Volume and Area Distributions in Porous Substances. I. Computations from Nitrogen Isotherms. *J. Am. Chem. Soc.* **1951**, *73* (2), 373–380.

(37) Makuła, P.; Pacia, M.; Macyk, W. How To Correctly Determine the Band Gap Energy of Modified Semiconductor Photocatalysts Based on UV-Vis Spectra. *J. Phys. Chem. Lett.* **2018**, *9* (23), 6814–6817. https://doi.org/10.1021/acs.jpclett.8b02892.

(38) Ravel, B.; Newville, M. Synchrotron Radiation ATHENA, ARTEMIS, HEPHAESTUS: Data Analysis for X-Ray Absorption Spectroscopy Using IFEFFIT. *J. Synchrotron Rad* **2005**, *12*, 537–541. https://doi.org/10.1107/S0909049505012719.

(39) Bartholomew, C. H. Mechanisms of Catalyst Deactivation. *Appl. Catal. A Gen.* **2001**, *212* (1–2), 17–60. https://doi.org/10.1016/S0926-860X(00)00843-7.

(40) Ueno, A.; Bennett, C. O. Infrared Study of CO2 Adsorption on SiO2. *J. Catal.* **1978**, *54* (1), 31–41. https://doi.org/10.1016/0021-9517(78)90024-6.

(41) Cordi, E. M.; Falconer, J. L. Oxidation of Volatile Organic Compounds on Al2O3, Pd/Al2O3, and PdO/Al2O3Catalysts. *J. Catal.* **1996**, *162* (1), 104–117. https://doi.org/10.1006/JCAT.1996.0264.

(42) Gulbransen, E. A.; Andrew, K. F.; Brassart, F. A. Oxidation of Molybdenum 550° to 1700°C. *J. Electrochem. Soc.* **1963**, *110* (9), 952. https://doi.org/10.1149/1.2425918.

(43) Hill, W.; Miessner, H.; Öhlmann, G. Fourier Transform Infrared Study of the Adsorption and of Reactions of Acetaldehyde on Dispersed Silica. *J. Chem. Soc. Faraday Trans. I* **1989**, *85* (3), 691–697. https://doi.org/10.1039/F19898500691.

(44) Socrates, G. *Infrared and Raman Characteristic Group Frequencies*; 2001. https://doi.org/10.1002/jrs.1238.

(45) Carosso, M.; Vottero, E.; Morandi, S.; Manzoli, M.; Ferri, D.; Fovanna, T.; Pellegrini, R.; Piovano, A.; Groppo, E. Deactivation of Industrial Pd/Al2O3 Catalysts by Ethanol: A Spectroscopic Study. *ChemCatChem* **2021**, *13* (3), 900–908. https://doi.org/10.1002/cctc.202001615.

(46) Seki, T.; Nakajo, T.; Onaka, M. The Tishchenko Reaction: A Classic and Practical Tool for Ester Synthesis. *Chemistry Letters*. The Chemical Society of Japan □ □ □ □ □ □ □ □ □ □ □ □ August 2006, pp 824–829. https://doi.org/10.1246/cl.2006.824.

(47) Biradar, A. V.; Umbarkar, S. B.; Dongare, M. K. Transesterification of Diethyl Oxalate with Phenol Using MoO 3/SiO2 Catalyst. *Appl. Catal. A Gen.* **2005**, *285* (1–2), 190–195. https://doi.org/10.1016/j.apcata.2005.02.028.

(48) Bañares, M. A.; Fierro, J. L. G.; Moffat, J. B. The Partial Oxidation of Methane on MoO3/SiO2 Catalysts: Influence of the Molybdenum Content and Type of Oxidant. *J. Catal.* **1993**, *142* (2), 406–417. https://doi.org/10.1006/jcat.1993.1218.

(49) Chakrabarti, A.; Wachs, I. E. Molecular Structure-Reactivity Relationships for Olefin Metathesis by Al2O3 -Supported Surface MoOx Sites. *ACS Catal.* **2018**, *8*, 949–959. https://doi.org/10.1021/acscatal.7b03598.

(50) Pelmenschikov, A. G.; Van Santen, R. A.; Jänchen, J.; Meijer, E. CD3CN as a Probe of Lewis and Bronsted Acidity of Zeolites. *J. Phys. Chem.* **1993**, *97* (42), 11071–11074. https://doi.org/10.1021/j100144a028.

(51) Escalona Platero, E.; Peñarroya Mentruit, M.; Morterra, C. Fourier Transform Infrared Spectroscopy Study of CD3CN Adsorbed on Pure and Doped γ-Alumina. *Langmuir* **1999**, *15* (15), 5079–5087. https://doi.org/10.1021/la981654c.

(52) Chakrabarti, A.; Wachs, I. E. Activation Mechanism and Surface Intermediates during Olefin Metathesis by Supported MoO x /Al 2 O 3 Catalysts. *J. Phys. Chem. C* **2019**, *123* (19), 12367–12375. https://doi.org/10.1021/acs.jpcc.9b02426.

(53) Xiao, L. P.; Wang, S.; Li, H.; Li, Z.; Shi, Z. J.; Xiao, L.; Sun, R. C.; Fang, Y.; Song, G. Catalytic Hydrogenolysis of Lignins into Phenolic Compounds over Carbon Nanotube Supported Molybdenum Oxide. *ACS Catal.* **2017**, *7* (11), 7535–7542. https://doi.org/10.1021/acscatal.7b02563.

(54) Delporte, P.; Meunier, F.́ de ́ric; Pham-Huu, C.; Vennegues, P.; Ledoux, M. J.; Guille, J. Physical Characterization of Molybdenum Oxycarbide Catalyst; TEM, XRD and XPS. *Catal. Today* **1995**, *23* (3), 251–267. https://doi.org/10.1016/0920-5861(94)00166-Y.

(55) Prasomsri, T.; Shetty, M.; Murugappan, K.; Román-Leshkov, Y. Insights into the Catalytic Activity and Surface Modification of MoO 3 during the Hydrodeoxygenation of Lignin-Derived Model Compounds into Aromatic Hydrocarbons under Low Hydrogen Pressures. *Energy Environ. Sci.* **2014**, *7* (8), 2660–2669. https://doi.org/10.1039/c4ee00890a.

(56) Rajagopal, S.; Marini, H. J.; Marzari, J. A.; Miranda, R. Silica-Alumina-Supported Acidic Molybdenum Catalysts - TPR and XRD Characterization. *J. Catal.* **1994**, *147* (2), 417–428. https://doi.org/10.1006/jcat.1994.1159.

(57) Tian, H.; Roberts, C. A.; Wachs, I. E. Molecular Structural Determination of Molybdena in Different Environments: Aqueous Solutions, Bulk Mixed Oxides, and Supported MoO3 Catalysts. *J. Phys. Chem. C* **2010**, *114* (33), 14110–14120. https://doi.org/10.1021/jp103269w.

(58) Hu, H.; Wachs, I. E.; Bare, S. R. Surface Structures of Supported Molybdenum Oxide Catalysts: Characterization by Raman and Mo Ls-Edge XANES. *J. Phys. Chem* **1995**, *99*, 10897–10910.

(59) Saraeian, A.; Burkhow, S. J.; Jing, D.; Smith, E. A.; Shanks, B. H. Catalyst Property Effects on Product Distribution during the Hydrodeoxygenation of Lignin Pyrolysis Vapors over MoO 3 /γ-Al 2 O 3 . *ACS Sustain. Chem. Eng.* **2021**, *9* (19), 6685–6696. https://doi.org/10.1021/acssuschemeng.1c00295.

(60) Rekoske, J. E.; Barteau, M. A. Kinetics, Selectivity, and Deactivation in the Aldol Condensation of Acetaldehyde on Anatase Titanium Dioxide. *Ind. Eng. Chem. Res.* **2011**, *50* (1), 41–51. https://doi.org/10.1021/ie100394v.

(61) Busca, G. Acid Catalysts in Industrial Hydrocarbon Chemistry. *Chem. Rev.* **2007**, *107* (11), 5366–5410. https://doi.org/10.1021/cr068042e.